Global and Planetary Change 215 (2022) 103875

Contents lists available at ScienceDirect

Global and Planetary Change

journal homepage: www.elsevier.com/locate/gloplacha

Reconstruction of the early Eocene paleoclimate and paleoenvironment of the southeastern Neo-Tethys Ocean

Yixin Dong [a,b], Liliana Calderón Convers [b], Shijun Jiang [c], Xiaona Li [b], Peng Zhu [d], Hongde Chen [a], Ying Cui [b,*]

[a] State Key Laboratory of Oil and Gas Reservoir Geology and Exploitation, Chengdu University of Technology, Chengdu 610059, China
[b] Department of Earth and Environmental Studies, Montclair State University, Montclair, NJ 07403, USA
[c] College of Oceanography, Hohai University, Nanjing 210024, China
[d] College of Energy Resources, Chengdu University of Technology, Chengdu 610059, China

ARTICLE INFO

Keywords:
Early Eocene
Southern Tibetan Plateau
Hyperthermal event
Chemical weathering intensity
Trace element geochemistry

ABSTRACT

The early Eocene is thought to be the warmest period of the Cenozoic Era, with global temperatures ~10 °C higher than today. Few studies have focused on the paleoclimatic history of the early Eocene southeastern Neo-Tethys Ocean despite its tectonic significance. Here, we report new geochemical data that reveal the paleoclimate conditions of the early Eocene (~ 53.7 to 52.6 Ma) from the Qumiba section in the Tingri region of the southern Tibetan Plateau, China, which likely represents the youngest marine strata in the southeastern Neo-Tethys Ocean. The studied Qumiba section consists of the Enba and Zhaguo Formations characterized by silty marls, mudstones and thin layers of lithic sandstones. The paleoclimate and paleoenvironment history of the Qumiba section is reconstructed using stable carbon and oxygen isotopes of marine carbonates ($\delta^{13}C_{carb}$ and $\delta^{18}O_{carb}$), major, trace and rare earth elements. At least one early Eocene hyperthermal event (I1 or I2; ~53.6 Ma) has been recorded in the Qumiba section supported by abrupt negative excursions in $\delta^{13}C_{carb}$ in Unit 2. This is further supported by enhanced chemical weathering (*e.g.*, chemical index of alteration), which can be attributed to increased temperature and precipitation. The continued negative $\delta^{13}C_{carb}$ excursions in Unit 3 may have been caused by the release of ^{13}C-depleted carbon from volcanic activities. The volcanic inputs may have increased nutrient availability and promoted marine primary productivity (*e.g.*, higher enrichment factors of P, Ba, Ni and Cu). Furthermore, the basin may have experienced bottom water anoxia as suggested by the redox-sensitive proxies (*e.g.*, higher enrichment factors of U and V and Ce/Ce*) during this period (Unit 3). Our findings support warming-induced changes in paleoenvironmental conditions in the southeastern Neo-Tethys Ocean during the early Eocene.

1. Introduction

A series of global warming events (~10^4–10^5 yrs. duration), termed early Eocene hyperthermals, occurred during the early Eocene (Ypresian; ~56 to 47.8 Ma) following the Paleocene-Eocene Thermal Maximum (PETM) (Abels et al., 2012; Cui and Schubert, 2017; Harper et al., 2020; Jiang et al., 2021; Leon-Rodriguez and Dickens, 2010; Littler et al., 2014; Nicolo et al., 2007; Slotnick et al., 2012; Stap et al., 2010). These hyperthermal events are characterized by higher global temperatures, fundamental perturbations to the global carbon cycle (*i.e.*, negative carbon isotope excursions), and other environmental effects (*e.g.*, dissolution of $CaCO_3$ in deep-sea sediments and enhanced chemical weathering on the continent). The collision of Indian and Asian plates in the early Eocene (~55–50 Ma) is considered one of the most notable tectonic events in the Cenozoic Era, which leaves indelible signatures in the sedimentary records in the eastern Neo-Tethys region. The continuous Late Cretaceous to Early Eocene shallow-marine stratigraphic sequence of the Tethyan Himalaya outcropped in southern Tibet provides an ideal archive to investigate the paleoenvironmental evolution of the southeastern Neo-Tethys Ocean and the climatic perturbations of the early Cenozoic (Hu et al., 2012; Li et al., 2017; Rowley, 1996; Wang et al., 2008; Zhang et al., 2017; Zhang et al., 2019). Recently, detailed biostratigraphic correlation and negative carbon isotope excursions (CIEs) in marine carbonates were utilized to recognize the PETM in the

* Corresponding author.
E-mail address: cuiy@montclair.edu (Y. Cui).

https://doi.org/10.1016/j.gloplacha.2022.103875
Received 15 September 2021; Received in revised form 14 June 2022; Accepted 15 June 2022
Available online 22 June 2022

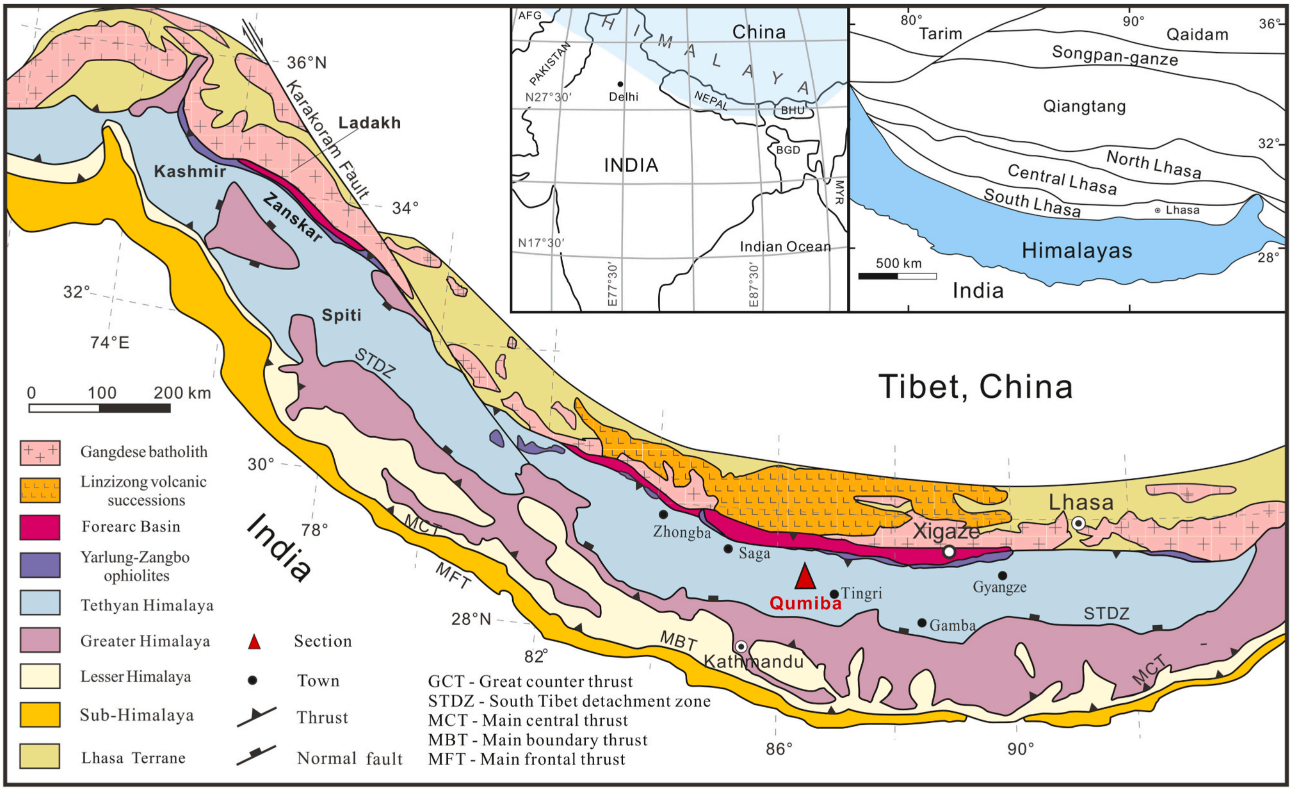

Fig. 1. Geological map of the Himalayas, modified from Hu et al. (2012) and Najman et al. (2017). The studied Qumiba section, shown as a red triangle, is located in the Tingri region in southern Tibet, China. The inset maps show the location of the Himalayas. (For interpretation of the references to colour in this figure legend, the reader is referred to the web version of this article.)

early Eocene Tethyan Himalaya (Li et al., 2017; Zhang et al., 2013; Zhang et al., 2019), but evidence for other early Eocene hyperthermals is still lacking.

Here, we present major and trace element data and stable isotopes of carbon and oxygen ($\delta^{13}C_{carb}$ and $\delta^{18}O_{carb}$) from the Qumiba section in southern Tibet of the Tethyan Himalaya across the early Eocene Enba and Zhaguo Formations (Fms.). We show that at least one of the early Eocene hyperthermal events are preserved in the sedimentary records of the Qumiba section through analyzing the geochemical characteristics of the mudstones deposited during the initial India-Asia collision. We use multiple geochemical proxies to identify the hyperthermal events and reconstruct the paleoenvironment changes of the southeastern Neo-Tethys Ocean before its final closure. Studying the early Eocene hyperthermals can provide important insights into the understanding of ongoing and future climate changes.

2. Geological settings

2.1. Tectonic settings and depositional environments

The southern Tibet is located in the Tethyan Himalaya of the northern Greater Indian continental margin (Fig. 1). Prior to the collision of Indian and Asian tectonic plates in the Eocene epoch (~55–50 Ma), this region was part of the interior Neo-Tethys Ocean in the Cretaceous and early Paleogene (Ding et al., 2016; Hu et al., 2016; Najman et al., 2017; Wang et al., 2008). The Neo-Tethys Ocean was considered to be initially formed in the late Early Permian (~270–260 Ma; Sengör, 1979; Zhu et al., 2021), and the collision of Indian and Asian tectonic plates led to the gradual closure of the Neo-Tethys Ocean, subsequent tectonic uplift, and the formation of the Tibetan Plateau (Spicer, 2021; Wang et al., 2008). Thus, the early Eocene successions recorded the depositional history immediately before the final closure of the southeastern Neo-Tethys Ocean (Najman et al., 2010).

The studied Qumiba section is located on the Zhepure Mountain in the Tingri region (GPS N28° 41′ 26″, E86° 43′ 37″, elevation 4924 to 4970 m; Fig. 1), which is ~60 km south of the Yarlung-Tsangpo suture in the Tethyan Himalaya in southern Tibet. Six stratigraphic units (from Lower Cretaceous to Eocene) have been identified in the Zhepure Mountain (Willems et al., 1996). The lower strata of the Gamba Group include Zhepure Shanbei Fm. and Zhepure Shan Fm., which are mainly composed of limestones and marls. The upper strata of the Gamba Group include Zhepure Shanpo Fm., Jidula Fm., Zongpu Fm. and Zongpubei Fm., which mainly consist of sandstones and mudstones. Zongpubei Fm. can be subdivided into the Enba and the Zhaguo Fms., which are mainly composed of mudstones (Hu et al., 2012; Wang et al., 2002; Willems et al., 1996; Zhu et al., 2005).

The studied interval covers the upper part of the Enba Fm. and the lower part of the Zhaguo Fm. The Enba Fm. consists of greenish-gray mudstones with thin interbedded sandstones (mainly litharenites), and has a thickness of approximately 105 m (Hu et al., 2012; Najman et al., 2010). The lithologic components of the sandstones consist mainly of volcanic rock fragments (Zhu et al., 2005). The sandstone beds become thicker and occur more frequently in the upper part of the Enba Fm., with horizontal, wavy cross-lamination and hummocky cross-stratified beds. The depositional environment of the upper Enba Fm. was storm-influenced outer shelf, in which the mudstones were formed by mud suspension settling and the sandstones by turbidity currents or high-energy events (Hu et al., 2012; Wang et al., 2002; Zhu et al., 2005). The overlying Zhaguo Fm. (~75 m) is composed of red mudstones and interbedded sandstones, similar to those of the Enba Fm. (Zhu et al., 2005). Thin sandstone beds in the Zhaguo Fm. are commonly characterized by a transgressive sequence, scoured bases, trough cross-lamination, horizontal lamination, and wavy cross-lamination, suggesting a shallow marine environment (Wang et al., 2002).

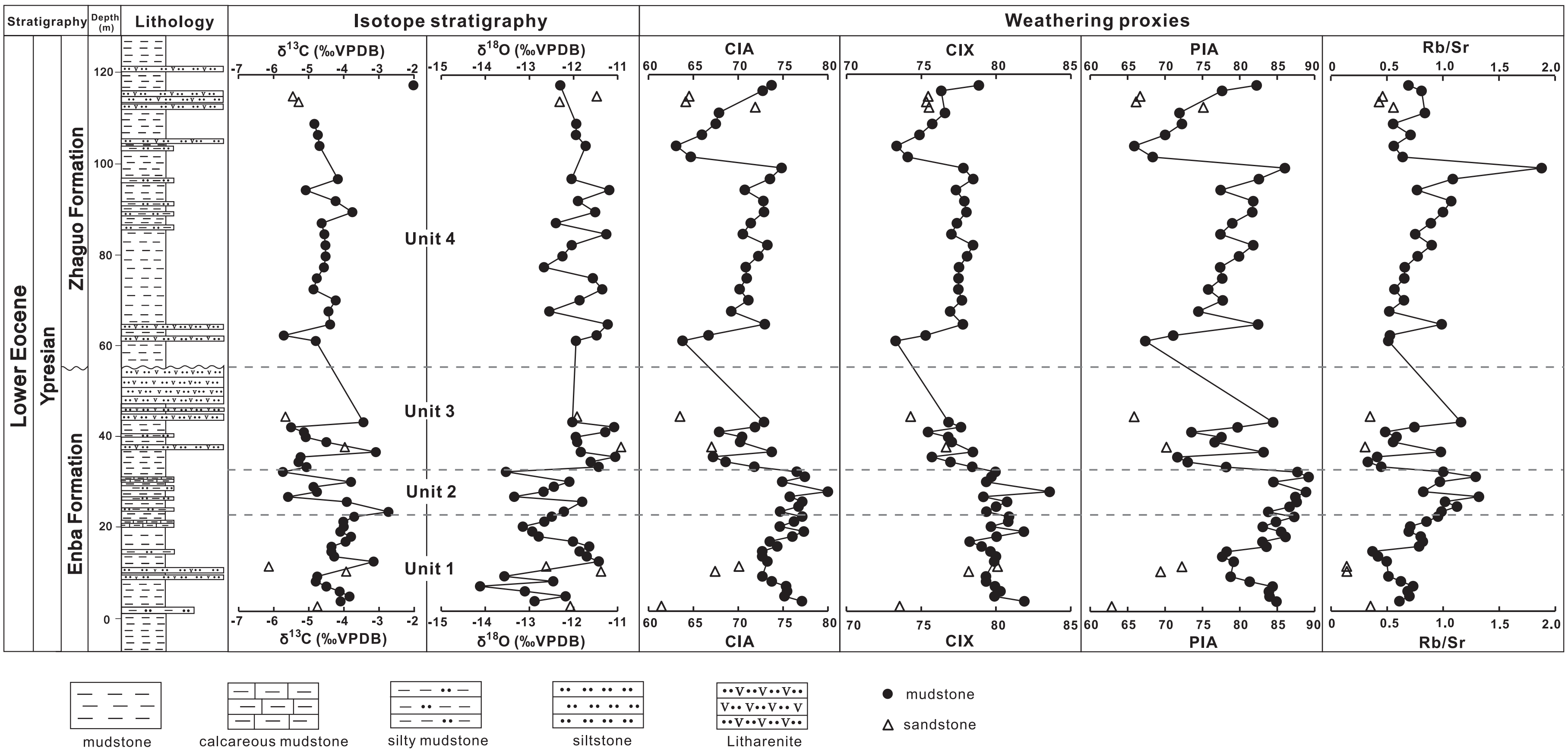

Fig. 2. The stratigraphic column of the Enba and Zhaguo Formations and stratigraphic distributions of the stable isotopes ($\delta^{13}C_{carb}$ and $\delta^{18}O_{carb}$) and weathering proxies of the Qumiba section. The weathering proxies include CIA, CIX, PIA and Rb/Sr. The four Units (Unit 1 to Unit 4) of the study interval are subdivided according to the carbon isotope stratigraphy.

2.2. Biostratigraphy and age constraints

The depositional ages of the Enba and Zhaguo Fms. are considered to be ~53.7–52.6 Ma (calcareous nannofossil biozone CNE3, Ypresian), evidenced by the calcareous nannofossil assemblages preserved in the two successions (Hoshina et al., 2021; Najman et al., 2010; Zhu et al., 2005). Calcareous nannoplankton are one of the most effective tools in biostratigraphy because they rapidly evolve over short geological time period and calcareous nannofossils can be identified easily in lithified samples to provide age constraints (Bown, 1998). Hoshina et al. (2021) performed detailed nannofossil counts on the sediments from the Enba and Zhaguo Fms. in the Qumiba section, and the Kernel Density Estimation (KDE) method was used to better constrain the age of sediments and recognize the reworked nannofossils in a stratigraphic layer. The Enba and Zhaguo Fms. are considered to form a continuous sequence, because no significant difference of the calcareous nannofossil assemblages is observed in the two successions (Hoshina et al., 2021; Najman et al., 2010), despite a subtle angular variation (≈11°) is observed between them (Najman et al., 2010). The youngest nannofossil assemblage components, including *Discoaster barbadiensis*, *Sphenolithus orphanknollensis*, *S. arthuri*, *D. kuepperi*, *Tribrachiatus orthostylus, Girgisia gammation*, *S. radians*, and *S. conspicuus*, represent Zone CNE3 (Eocene calcareous nannofossil biozone). The absence of *Discoaster lodoensis* (a marker of CNE4) and some *reticulofenestrids* (*i.e.*, *Dictyococcites*, *Reticulofenestra* and *Cyclicargolithus*) constrain the age up to 52.64 Ma. Additionally, the youngest zircon ages of the sandstones from the Enba and Zhaguo Fms. are 54 ± 1 Ma and 53 ± 1 Ma (2% discordance) respectively in the nearby Gamba area (Li et al., 2015), further supporting the age of the deposition of Enba and Zhaguo Fms. to be within ~53.7–52.6 Ma.

3. Material and methods

A total of 65 freshly excavated outcrop samples, including eight sandstones and 57 mudstones, were collected from the Enba Fm. and the Zhaguo Fm. in the Qumiba section for this study, with an average sampling interval of ~1 m (Tables S1 and S2). We removed the possible contaminants on the surface of samples by cutting the outmost weathered materials and washing the samples by ethanol to ensure the cleanness of the samples. Afterwards, all samples were ground to powder using a SPEX zirconia ceramics ball mill for geochemical analyses.

3.1. Stable carbon and oxygen isotope analyses

The analyses of inorganic carbon ($\delta^{13}C_{carb}$) and oxygen isotopes ($\delta^{18}O_{carb}$) from marine carbonates were performed at the Key Laboratory of Submarine Geosciences of the Second Institute of Oceanography in Hangzhou, China, using a Thermo Finnigan Delta Plus AD mass spectrometer interfaced to a GasBench II Auto-Carbonate device. After freeze drying and homogenizing the pretreated samples, each sample with suitable weight was selected and reacted with 100% phosphoric acid (H_3PO_4) at 72 °C overnight. Subsequently, the carbon and oxygen isotopic ratios were measured using the mass spectrometer. The CO_2 gas in the reference cylinder was calibrated with references (NBS-19, GBW04406 and GBW04405). All the results were reported relative to the Vienna Pee Dee Belemnite standard (VPDB), and the analytical precision (1σ) is ±0.1‰ for $\delta^{13}C_{carb}$ and ± 0.3‰ for $\delta^{18}O_{carb}$. The magnitudes of CIEs are calculated as the difference between average pre-excursion isotopic values and the minimum values.

3.2. Major and trace element analyses

The major and trace elements (including rare earth elements; REEs) were analyzed using an ICAP Q Inductively Coupled Plasma – Mass Spectrometry (ICP-MS) housed at the Department of Earth and Environmental Studies at Montclair State University, NJ, United States. For each homogenized sample, around 100 mg of powder were mixed with 400 mg of ultrahigh-purity lithium metaborate flux ($^{(R)}$Spex-Certiprep) and fused in high-purity graphite crucibles at 1050 °C for 40 min in the Thermo Scientific™ Lindberg/Blue M™ Box Furnace. Afterwards, molten samples were dissolved in 50 ml of 7% HNO_3, and then prepared for a second dilution of the sample using 2% HNO_3 (dilution factor of ~10,000×) before ICP-MS analysis. Additional blanks were prepared to correct for any analytical signals from the sample treatment. An instrument calibration curve was calculated using ten rock standards of the U.S. Geological Survey (USGS) (BIR-1, DNC-1, QLO-1, RGM-1, AGV-2, BCR-2, BHVO-2, G-2, GSP-2, and W-2). The reported results were the average values of three analytical runs by the ICP-MS for all the samples. The analytical precision (1σ) for all elements is better than 10%.

Multiple weathering proxies were examined *via* the molar proportions of major oxides and subsequently used to detect chemical weathering intensities (Fig. 2). The most widely used chemical weathering proxy is Chemical Index of Alteration (CIA), calculated as: CIA = $[Al_2O_3/(Al_2O_3 + CaO^* + Na_2O + K_2O)] \times 100$ (molar proportions), to express the transformation degree of feldspars to clays during chemical weathering processes (Nesbitt and Young, 1982). The CaO* refers to the CaO molar proportions in the silicate fractions of the rock other than in the apatite and/or carbonate fractions (Fedo et al., 1995), which is calculated as: $CaO^* = \min(CaO - 10/3 \times P_2O_5, Na_2O)$ (McLennan, 1993; Panahi et al., 2000). Other chemical weathering proxies involve modified Chemical Index of Alteration (CIX = $[Al_2O_3/(Al_2O_3 + Na_2O + K_2O)] \times 100$; Garzanti et al., 2014) and Plagioclase Index of Alteration (PIA = $[(Al_2O_3 - K_2O) / (Al_2O_3 + CaO^* + Na_2O - K_2O)] \times 100$; Fedo et al., 1995). To normalize the results and describe the enrichment degree of the environmentally sensitive elements, enrichment factors (EF) of selected elements were calculated as: $X_{EF} = (X/Al)_{sample}/(X/Al)_{average\ shale}$, where X represents the concentrations of the element of interest and the concentrations of average shale are from Wedepohl (1991). All the measured concentrations of REEs were normalized to the Post-Archean Australian Shale (PAAS; Pourmand et al., 2012). Ce anomalies were calculated according to Bau and Dulski (1996): $Ce/Ce^* = (2 \times Ce_{SN})/(La_{SN} + Pr_{SN})$, where SN stands for shale-normalized value.

4. Results

4.1. Stable carbon and oxygen isotopes

The Enba and Zhaguo Fms. of the Qumiba section are subdivided into four units (Unit 1, 0–22 m; Unit 2, 22–32.5 m; Unit 3, 32.5–60 m; Unit 4, 60–120 m) based on $\delta^{13}C_{carb}$ chemostratigraphy. The $\delta^{13}C_{carb}$ values of the mudstones in the Enba and Zhaguo Fms. vary from −5.7 to −2.0‰ (average −4.4‰), and the $\delta^{18}O_{carb}$ values are from −14.1 to −11.2‰ (average −12.1‰) (Table S1; Fig. 2). The low $\delta^{18}O_{carb}$ values may be partly attributed to the impact of meteoric water and early diagenesis (Table S1), which limits their usage as surface temperature proxy. The $\delta^{13}C_{carb}$ values display significant variations in Unit 2 and Unit 3, and fluctuate slightly in Unit 1 and Unit 4. The $\delta^{13}C_{carb}$ values start to decrease from −3.9‰ at 25.2 m to its minimum value of −5.7‰ at 31.7 m in Unit 2 and then abruptly return to background values of ~ −3.1‰ at 36.1 m, bracketing a ~ 11 m interval. Similarly, $\delta^{18}O_{carb}$ records show a negative 1.7‰ shift in Unit 2. The negative shift of $\delta^{13}C_{carb}$ continues in a ~ 10 m interval in Unit 3 (minimum value is −5.5‰) with no accompanying negative shift of $\delta^{18}O_{carb}$ (Fig. 2).

4.2. Major element geochemistry

The mudstone samples of the Enba and Zhaguo Fms. are mainly composed of SiO_2 (61.2–73.2%), Al_2O_3 (12.3–19.8%), Fe_2O_3 (3.9–11.3%), CaO (0.4–7.3%), MgO (1.7–3.5%), K_2O (0.7–4.0%), and Na_2O (0.6–1.7%), with low contents of TiO_2 (<1.0%), MnO (<0.3%), and P_2O_5 (<0.2%). The CaO content (average 3.7%) is slightly higher than that of the upper continental crust (UCC; 2.2%) (Taylor and McLennan, 1985). The contents of SiO_2, Al_2O_3, TiO_2, CaO, Na_2O, and

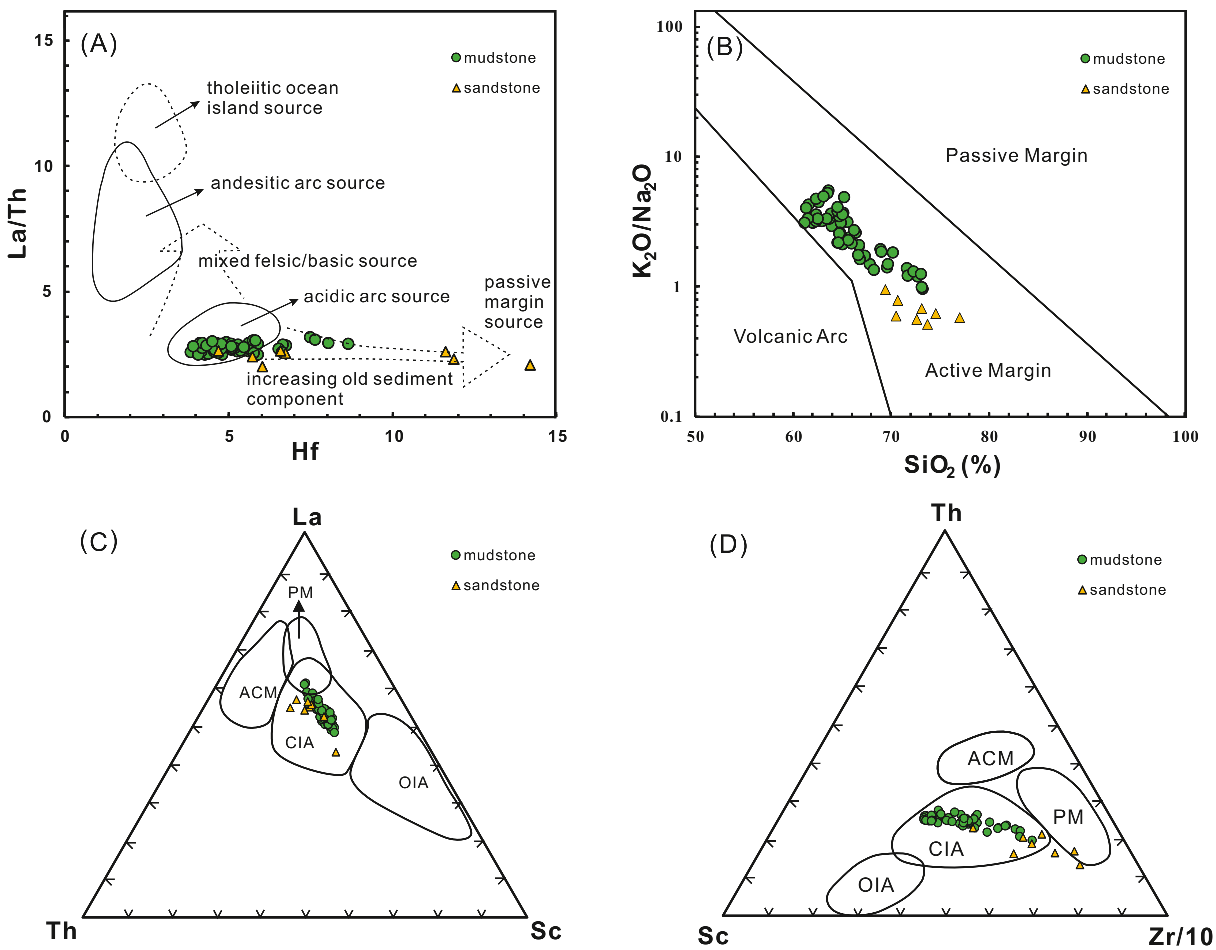

Fig. 3. Ternary discrimination diagrams for the mudstone and sandstone samples of the early Eocene Enba and Zhaguo Formations. (A) La/Th *versus* Hf diagram (after Floyd and Leveridge, 1987); (B) K_2O/Na_2O *versus* SiO_2 diagram (after Roser and Korsch, 1986); (C) La-Th-Sc ternary diagram (after Bhatia and Crook, 1986); (D) Th-Sc-Zr/10 ternary diagram (after Bhatia and Crook, 1986); OIA: oceanic island arc; CIA: continental island arc; ACM: active continental margin; PM: passive margin.

K_2O change abruptly between Unit 2 and Unit 3, with SiO_2, TiO_2, CaO, Na_2O showing increasing trends and Al_2O_3 and K_2O exhibiting decreasing trends. The contents of Fe_2O_3 and MnO remain relatively stable over the entire section with small variations (Table S2). All the weathering proxies (CIA, CIX and PIA) exhibit similar trends, with low values in Unit 1, slightly higher values in Unit 2, reduced values in Unit 3 and relatively stable values in Unit 4 (Fig. 2).

4.3. Trace element geochemistry

The enrichment factors (X_{EF}) of various trace elements can be used to track changes of source materials (*e.g.*, Zr_{EF}, Cr_{EF}), paleoproductivities (*e.g.*, P_{EF}, Ba_{EF}, Ni_{EF}, Cu_{EF}) and redox conditions (*e.g.*, U_{EF}, V_{EF} and Ce/Ce*) (Shen et al., 2015; Takahashi et al., 2014; Tribovillard et al., 2006). The values of Zr_{EF} and Cr_{EF} remain low throughout the entire section, but increase abruptly from 1.0 to 2.6 and 1.0 to 2.3 in the 32.9–41 m interval in Unit 3, which is similar to the trends of Ti_{EF} (Fig. 4). Productivity-sensitive proxies (P_{EF}, Ba_{EF}, Ni_{EF} and Cu_{EF}) decrease slightly from 0 to 32.9 m in Unit 1 and Unit 2, then increase sharply and reach their maximum values of 0.48, 1.48 and 1.74 in Unit 3, and stay relatively low and stable in Unit 4 (Fig. 5). The redox-sensitive proxies (U_{EF} and V_{EF}) show low values across most of the section, but display higher values of 0.7–1.2 and 1.0–1.4 from 32.9 to 41 m in Unit 3 (Fig. 5).

The PAAS normalized REE patterns can also track sediment source changes. Three types of REE patterns are identified, in which mudstones display Type 1 and Type 2 patterns and sandstones display Type 3 pattern (Fig. 4). The main difference between Type 1 and Type 2 mudstones is that Type 1 mudstones have lower Er_{SN}/Tm_{SN} ratios (0.81–1.93; average 0.94) than those of Type 2 mudstones (0.61–0.89; average 0.78). The major difference between mudstones and sandstones in their REE patterns is that the light rare earth elements (LREEs) of sandstones are more depleted than those of mudstones. Stratigraphically speaking, most of the Type 2 mudstones are found in Unit 1 and Unit 2. The Ce/Ce* ratios vary within a small range from 0.94 to 1.07, and a decrease from 1.02 to 0.94 is seen from 32.9 to 41 m in Unit 3, which exhibits an opposite trend compared to U_{EF} and V_{EF} data (Figs. 4 and 5).

5. Discussion

5.1. Sediment provenance

The tectonic features and provenance of the sediments from the Enba and Zhaguo Fms. can provide important information on the final stage of sedimentation of the Neo-Tethys Ocean during the initial collision between the Indian and Asian tectonic plates (Hu et al., 2012; Wang et al., 2008). Mudstones are considered to preserve the elemental components of the source rocks (Bhatia and Crook, 1986; Cullers, 2002; Garver and Scott, 1995; McLennan and Taylor, 1991), so our discussions on sediment provenance will focus on geochemical data from mudstones, rather than sandstones.

The tectonic classification diagram of mudstones (SiO_2 content *vs.* log (K_2O/Na_2O)) can help differentiate tectonic settings, because the

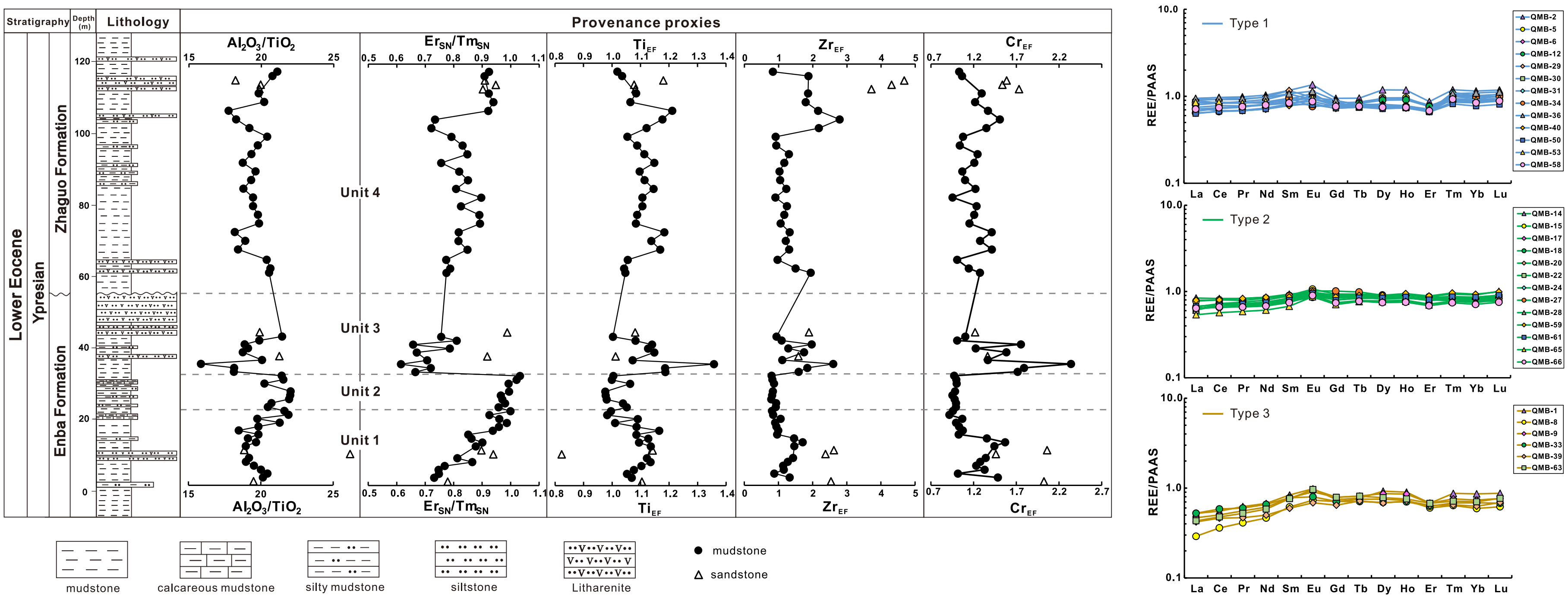

Fig. 4. Stratigraphic distributions of provenance proxies and REE patterns of the Qumiba section. The provenance proxies include Al_2O_3/TiO_2 ratio, Er_{SN}/Tm_{SN} ratio, Ti_{EF}, Zr_{EF} and Cr_{EF}. The REE patterns of sandstone and mudstone samples are divided into three types, Type 1, Type 2 and Type 3.

SiO_2 contents and K_2O/Na_2O ratios of sediments increase systematically from volcanic arc to active continental margins, followed by passive margins (Roser and Korsch, 1986). All mudstones from the Enba and Zhaguo Fms. are plotted within the active margin field, in the vicinity of the volcanic arc field (Fig. 3B), suggesting that the sediments were most likely sourced from an active tectonic setting. This inference is further supported by trace element geochemistry, such as La, Sc, Th, Zr, and Hf, which are indicators of tectonic settings due to their resistance to changes by weathering and transport processes (Bhatia and Crook, 1986; McLennan and Taylor, 1991). All the mudstone samples fall into the continental island arc (CIA) field in the La-Th-Sc and Th-Sc-Zr/10 ternary diagrams and La/Th *vs.* Hf content diagram (Fig. 3), supportive of a relatively active tectonic background. The tectonic interpretation of the geochemical data for the Enba and Zhaguo Fms. is in agreement with Zhu et al. (2005) and Li et al. (2015), who suggest that the lithic components of sandstones from the Enba and Zhaguo Fms. were derived from the magmatic arc north of the Tethyan Himalaya (*i.e.*, north Asian active margin) with similar properties of the volcanic rocks from the Lhasa terrane.

Although the tectonic features of the Enba and Zhaguo Fms. are similar, the sources of sediments may differ. The Al_2O_3/TiO_2 ratio is a widely used provenance indicator because both Al and Ti are immobile during sediment transport and weathering processes (Sugitani et al., 1996; Young and Nesbitt, 1998). Across the Qumiba section, the Al_2O_3/TiO_2 ratios of most samples remain steady in Unit 1, Unit 2 and Unit 4, with the exception of a sharp decrease in Unit 3 (Fig. 4), indicating a rapid change in sediment provenance. Meanwhile, the sharp increase in Ti_{EF}, Zr_{EF} and Cr_{EF} values in Unit 3 suggest the influence of additional sources, because Ti, Zr and Cr are often associated with heavy minerals, which are the most immobile elements during chemical weathering (Hayashi et al., 1997; Scheffler et al., 2003; Zhou et al., 2015). Additionally, the distribution patterns of REEs further support a change in sediment provenance in the lower part of Unit 3 (Fig. 4). REEs can largely preserve the geochemical information of the source rocks, because they are relatively stable and barely influenced by weathering, transport, and diagenetic processes of sediments (Murray et al., 1990; McLennan, 2018). All the mudstone samples show a similar REE pattern, except for the Er_{SN}/Tm_{SN} ratios (Fig. 4). The abrupt decrease of Er_{SN}/Tm_{SN} ratios in Unit 3 may be attributed to changes in the source rocks, because Er and Tm are the most inert elements among the REEs (McLennan, 1994; McLennan, 2018). Similarly, the mudstone samples in Unit 2 exhibit the Type 2 REE pattern and those in Unit 3 display the Type 1 REE pattern (Fig. 4), suggesting a change in sediment provenance from Unit 2 to Unit 3, which may be attributed to the inputs from volcanic activities during Unit 3 (discussed in 5.3).

5.2. Recognition of early Eocene hyperthermal events

Several lines of evidence support the presence of early Eocene hyperthermal events I1 or I2 in the studied section. First, $\delta^{13}C_{carb}$ and $\delta^{18}O_{carb}$ show significant negative excursions in Unit 2, with a maximum magnitude of ~1.8‰ and ~1.7% respectively, which indicates ^{13}C-depleted carbon emissions and higher sea surface temperature. Despite the low CaO content (0.4 to 7.3%, Table S2), the abundant calcareous nannofossils likely provided the calcite minerals needed for the measurement of $\delta^{13}C_{carb}$ and $\delta^{18}O_{carb.}$ The Unit 2 intervals could potentially capture I1 or I2 event because biostratigraphy shows that the negative CIEs occurred within the calcareous nannofossil biozone CNE3 (Section 2.2). However, ETM2 is unlikely to be preserved due to the absence of nannofossil excursion taxa (*e.g.*, *Rhomboaster* and *Discoaster araneus*) at the study site. This is because these nannofossil taxa have been reported to occur only during the PETM and ETM2 because of their adaptation to the rapidly and severely changing surface-water environment (Jiang and Wise Jr, 2006; Kahn and Aubry, 2004; Lei et al., 2016; Raffi and De Bernardi, 2008; Self-Trail et al., 2012). As a result, the geochemical features observed in Unit 2 are consistent with the characteristics of the I1/I2 event (*e.g.*, ~53.6 Ma) (Abels et al., 2012; Cui and Schubert, 2017; Harper et al., 2020; Jiang et al., 2021; Leon-Rodriguez and Dickens, 2010; Littler et al., 2014; Stap et al., 2010), which led to the suggestion that at least one of the early Eocene hyperthermals may have been recorded in the southeastern Neo-Tethys region. Due to the uncertainty of the age based on biostratigraphy at the study site, we are unable to specify whether the hyperthermal event recorded is I1 or I2.

Hyperthermal events are often accompanied by enhanced chemical weathering (Hessler et al., 2017; Jiang et al., 2021; Kemp et al., 2020; Kump et al., 2000; Ravizza et al., 2001). We evaluated the changes in weathering intensity in the Enba and Zhaguo Fms. using chemical weathering proxies (*e.g.*, CIA, CIX, PIA), which increase significantly in Unit 2 corresponding to the negative excursions of $\delta^{13}C_{carb}$ and $\delta^{18}O_{carb}$ (Fig. 2). The chemical weathering intensity reflects 1) the magnitude of the dissolution of minerals and rocks (Von Blanckenburg, 2005); 2) the removal of ions by subaerial or surficial aqueous reactions (Riebe et al., 2004; West et al., 2005); and 3) processes dominated by feldspar degradation and associated formation of clay minerals (Dellinger et al., 2017; Nesbitt and Young, 1982; Von Blanckenburg, 2005), which largely depend on the climatic conditions (Nesbitt and Young, 1982; Schoenborn and Fedo, 2011). The values of these weathering proxies increase with the intensity of chemical weathering, because refractory elements (*e.g.*, Al and Ti) are commonly retained while soluble elements (*e.g.*, Ca, Na, and K) are preferentially leached out from feldspars during weathering processes (Fedo et al., 1995; Nesbitt and Young, 1982; Sheldon and Tabor, 2009). Furthermore, the enhanced chemical weathering is supported by an increase in Rb/Sr ratios from 25 to 31 m in Unit 2 (Fig. 2). This is because the inert Rb commonly replaces K and remains at clay mineral exchange sites, while Sr is preferentially removed during weathering processes (Chen et al., 1999; El Bouseily and El Sokkary, 1975; Jin et al., 2006). The increased values of these chemical weathering proxies and Rb/Sr ratios may indicate a warmer and more humid climatic condition during this time (Unit 2), which could significantly enhance the chemical weathering intensity of the source rocks. This could be due to an enhanced hydrological cycle from higher atmospheric pCO_2 and temperature during the early Eocene hyperthermals (Hessler et al., 2017; Jiang et al., 2021; Kemp et al., 2020; Krishnan et al., 2014; Kump et al., 2000; Ravizza et al., 2001). Increase in chemical weathering intensity agrees well with the characteristics of the hyperthermal event (Fig. 2). A similar increase in weathering intensity during the early Eocene hyperthermal events has been found globally, including New Zealand (Slotnick et al., 2012), Ocean Drilling Program Site 1258 in the tropical Atlantic (Jiang et al., 2021), and Site 1265 in the South Atlantic (Dedert et al., 2012).

5.3. Volcanic activities in Unit 3

In the early Eocene, numerous tectonomagmatic activities occurred in southern Tibet due to the subduction of the Neo-Tethyan oceanic plate during the initial stage of the India-Asia collision (Kohn and Parkinson, 2002; Lee et al., 2009; Mahéo et al., 2002). Volcanic activities are supported by the increase in volcanic rock fragments in the sandstones of the upper Enba Fm. (Li et al., 2015; Zhu et al., 2005) and large increase in Ti_{EF}, Cr_{EF}, and Zr_{EF} in Unit 3 (Fig. 4), because Ti, Cr, and Zr are associated with heavy minerals from volcanic sources (Khozyem et al., 2013; Pujol et al., 2006; Yang et al., 2020). Volcanic activities can also be inferred from the reduced CIA values from 75 to 67 in Unit 3, which cannot be explained by the decline of chemical weathering intensity alone. This is because the CIA values can also be affected by both variations of source rock compositions and post-depositional diagenesis, especially potassium metasomatism (Fedo et al., 1995; Nesbitt and Young, 1982; Xu et al., 2017; Yang et al., 2016). The role of potassium metasomatism in affecting the CIA values is thought to be limited in the study interval, because the mudstones in the Enba and Zhaguo Fms. largely follow the ideal weathering trend in the A-CN-K ternary diagram and do not follow the K-metasomatism trend (Fig. 6A) (Critelli et al.,

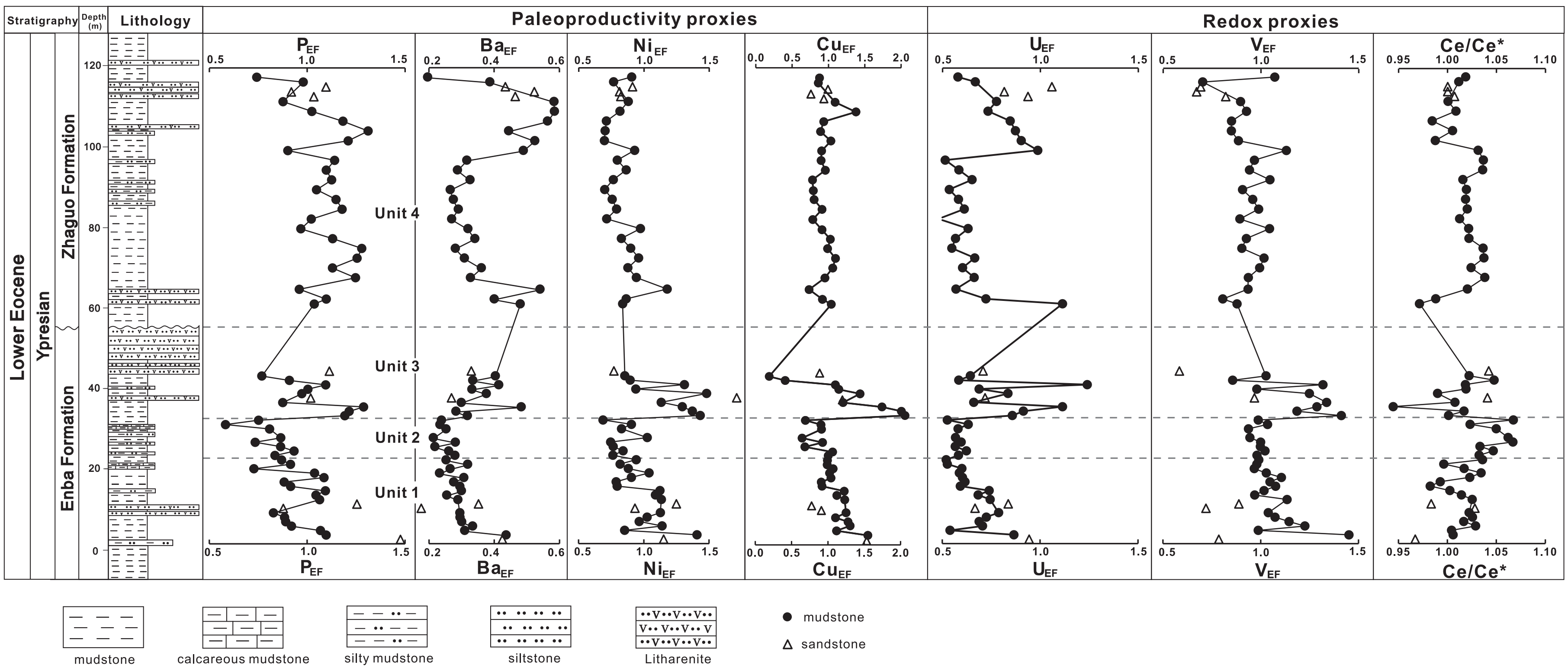

Fig. 5. Stratigraphic distributions of paleoproductivity proxies (P_{EF}, Ba_{EF}, Ni_{EF} and Cu_{EF}) and redox proxies (U_{EF}, V_{EF} and Ce/Ce*).

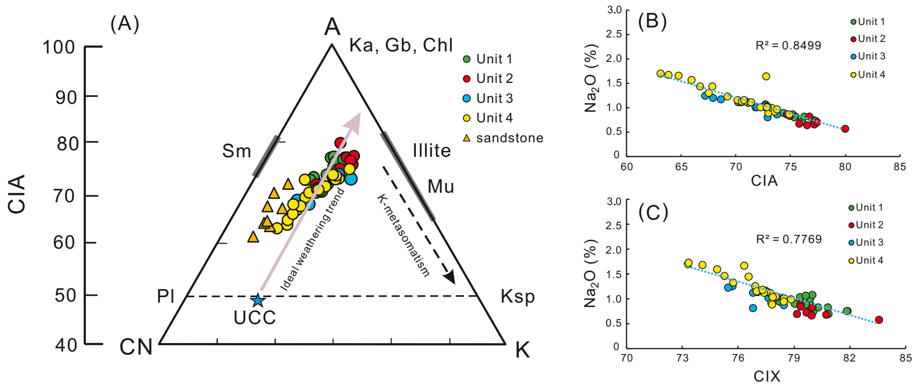

Fig. 6. (A) Ternary diagram of Al_2O_3-(CaO* + Na_2O)-K_2O (A-CN-K) of the samples in the Qumiba section (after Nesbitt and Young, 1984). The UCC (upper continental crust) datapoint is from Taylor and McLennan (1985). Pl: plagioclase; Ksp: K-feldspar; Sm: smectite; Mu: muscovite; Ka: kaolinite; Gb: gibbsite; Chl: chlorite; (B) Negative correlation between Na_2O content and CIA values for mudstone samples in the Qumiba section; (C) Negative correlation between Na_2O content and CIX values for mudstone samples in the Qumiba section.

2008; Fedo et al., 1995; Wang et al., 2020; Nesbitt and Young, 1984; Yang et al., 2018). Therefore, we suggest that the addition of volcanic-sourced Na may have led to the decrease in CIA values in Unit 3. This is partly because the Na_2O contents of mudstones are negatively correlated with the CIA values ($r^2 = 0.85$, $P < 0.001$) and CIX values ($r^2 = 0.78$, $P < 0.001$) (Fig. 6B, C). The increase of Na_2O content may be related to the addition of smectites, which are the primary weathering products of basaltic materials (Babechuk et al., 2014; Eggleton et al., 1987). Alternatively, the orogenic uplift that occurred during this period (Lee et al., 2009; Wang et al., 2008) may have enhanced physical weathering (*e.g.*, erosion, denudation, frost shattering), and reduced chemical weathering and lowered the CIA values (Dinis et al., 2020; Liu et al., 2017; Riebe et al., 2004; West et al., 2005). Therefore, it is likely that the decrease in CIA is related to the addition of Na from volcanic activities near the study site or through physical weathering processes.

As a result of volcanic activities, marine primary productivity can be promoted by increased input of bio-essential elements, such as P, Fe, Ni and Cu (Hamme et al., 2010; Schoepfer et al., 2015; Shen et al., 2015). The concurrent increase in P_{EF} and Ba_{EF} supports enhanced primary productivity in Unit 3 in the Qumiba section (Fig. 5; lower part of Unit 3). P is an essential nutrient element for the growth of marine organisms, and Ba is closely related to the primary productivity in the surface water and the export of organic matter (McManus et al., 1998; Schoepfer et al., 2015; Tribovillard et al., 2006). Although surface primary productivity is shown to be positively correlated with the P_{EF} and Ba_{EF} proxies, they can be affected by bulk sediment accumulation rates and bottom water redox conditions (Paytan and Griffith, 2007; Schoepfer et al., 2015; Tribovillard et al., 2006; Yang et al., 2020). Therefore, Ni_{EF} and Cu_{EF} proxies are used in addition to P_{EF} and Ba_{EF} to further support the development of increased primary productivity. As micronutrients, Ni and Cu can be adsorbed onto organometallic complexes and delivered to the sediments, and can be served as proxies for paleoproductivity (Horner et al., 2021; Tribovillard et al., 2006). As a result, the concurrent increase of the P_{EF}, Ba_{EF}, Ni_{EF} and Cu_{EF} in Unit 3 support increased marine primary productivity during this time.

Higher paleoproductivity can lead to the expansion of the oxygen minimum zones (OMZs) and anoxic bottom waters (Algeo and Ingall, 2007; Dahl and Arens, 2020; Ozaki et al., 2011; Van Cappellen and Ingall, 1996). Decrease in oxygen in bottom waters through oxygen-productivity feedbacks in the study site is supported by the increase in U_{EF} and V_{EF} values, and the decrease in Ce/Ce* ratios in Unit 3 in the Qumiba section (Fig. 5). Under reducing conditions, soluble U and V can be reduced to insoluble chemical compounds and be removed from the water column to the sediments, leading to enrichment of U and V in the sediments (Takahashi et al., 2014; Tribovillard et al., 2006). The lower Ce/Ce* ratio in Unit 3 provides further support to the inferred anoxic bottom waters, because the insoluble Ce (IV) can be reduced to soluble Ce (III) under oxygen-depleted conditions, leading to the removal of oxidized Ce (IV) in the sediments and a decrease in Ce/Ce* ratio (Bau and Koschinsky, 2009; German and Elderfield, 1990; Nakada et al., 2016). In summary, enhanced volcanic activities on the Lhasa terrane may have increased the paleoproductivity of the surface ocean and enhanced bottom water anoxia at the study location in the southeastern Neo-Tethys Ocean (Fig. 7C).

5.4. Comparison of global I1/I2 records

The early Eocene hyperthermals are characterized by global carbon and oxygen isotope excursions, driven by ^{13}C-depleted CO_2 emissions (Abels et al., 2012; Cui and Schubert, 2017; Harper et al., 2020; Leon-Rodriguez and Dickens, 2010; Stap et al., 2010). I1/I2 hyperthermal events are prominent global warming events just before the long period of the early Eocene climatic optimum (EECO), but has a smaller degree of warming compared to the PETM and ETM2 (Cramer et al., 2003; Nicolo et al., 2007; Lauretano et al., 2015; Cui and Schubert, 2017). At present, the I1/I2 events have been documented in multiple pelagic-hemipelagic sequences, such as the DSDP (Deep Sea Drilling Project) Site 577 and ODP (Ocean Drilling Program) Site 1209 at Shatsky Rise in the central Pacific (Cramer et al., 2003; Westerhold et al., 2018), DSDP Site 550 and ODP Site 1051 in the northern Atlantic (Cramer et al., 2003), ODP Site 1258 at Demerara Rise in the western equatorial Atlantic (D'Onofrio et al., 2020; Sexton et al., 2006), ODP Sites 1262 and 1263 at Walvis Ridge in the south Atlantic (Lauretano et al., 2015; Littler et al., 2014; Zachos et al., 2010), ODP Site 1215 near Hawaii in the central Pacific (Leon-Rodriguez and Dickens, 2010), Terche and Possagno sections in Southern Alps in Italy (D'Onofrio et al., 2016; Galeotti et al., 2019), Contessa section in the central Italy (Francescone et al., 2019; Galeotti et al., 2010). A few I1/I2 records are found in shallow marine sequences, including Mead and Dee Stream in New Zealand (Nicolo et al., 2007; Slotnick et al., 2012), and Galala platform in the Egyptian shelf (Höntzsch et al., 2011). Several terrestrial sequences, including the Fushun Basin in China (Chen et al., 2014), the Bighorn Basin in Wyoming (Abels et al., 2016), the Vastan and Valia sections in western India (Samanta et al., 2013), and Ellesmere Island in the Canadian Arctic (Reinhardt et al., 2022) also recorded the I1/I2 (Fig. 8; Table S3).

In general, the $\delta^{13}C_{carb}$ values of the Qumiba section are similar to those of the siliciclastic dominated shallow marine sequences (−4 to 2‰; note that the Eocene $\delta^{13}C_{carb}$ values are generally lower than Paleocene values) of the Egyptian shelf on the southern Tethyan carbonate platform (Höntzsch et al., 2011), but lower than those observed at other pelagic-hemipelagic sites. The relatively low $\delta^{13}C_{carb}$ values may be due to organic matter remineralization within the sediments and early diagenesis (Meyers, 1994; Rullkötter, 2006). In addition, the inputs of reworked Cretaceous calcareous nannofossils (Hoshina et al., 2021) could also distort the original $\delta^{13}C$ signal (D'Onofrio et al., 2016), which may complicate the interpretation of the $\delta^{13}C$ data. However, the relative changes in $\delta^{13}C_{carb}$ are likely minimally impacted by these

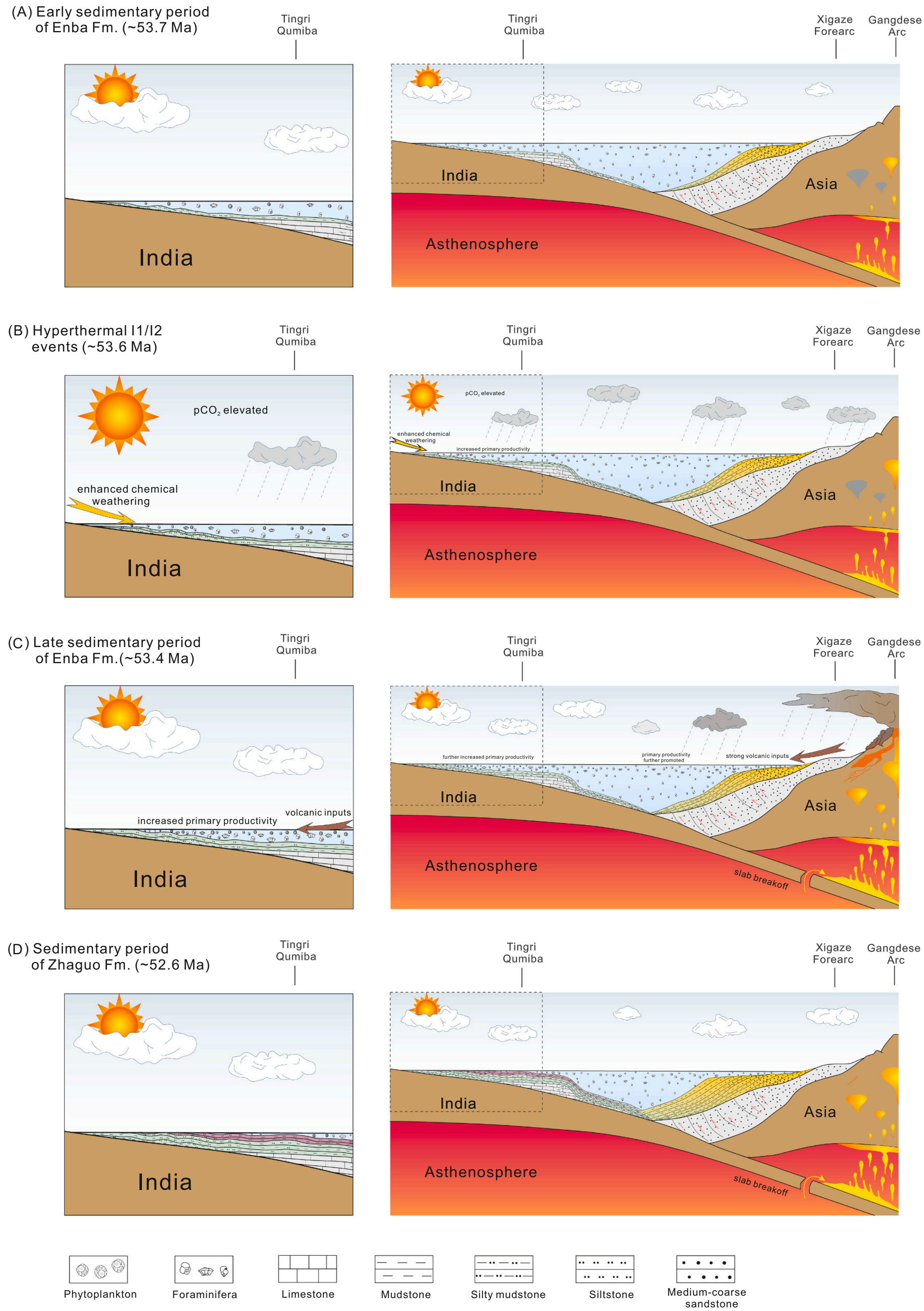

Fig. 7. Interpreted sedimentary models of the early Eocene Enba and Zhaguo Formations at the Qumiba section in the Tingri area (left images) and in southern Tibet (right images; modified from Hu et al., 2012 and Lee et al., 2009); (A) During the early sedimentary period of the Enba Fm., the depositional environment of the Qumiba section was the storm-influenced outer shelf with the mudstone sediments; (B) During the hyperthermal event I1/I2, chemical weathering was enhanced due to elevated pCO_2 and temperature; (C) During the late sedimentary period of the Enba Fm., strong volcanic inputs from the Lhasa terrane occurred, which were caused by the incipient India–Asia collision, rollback and breakoff of the subducted oceanic slab, leading to the increased primary productivity and the expansion of anoxic conditions; (D) During the sedimentary period of the Zhaguo Fm., the southeastern Neo-Tethys Ocean was gradually filled by the shallow marine sediments.

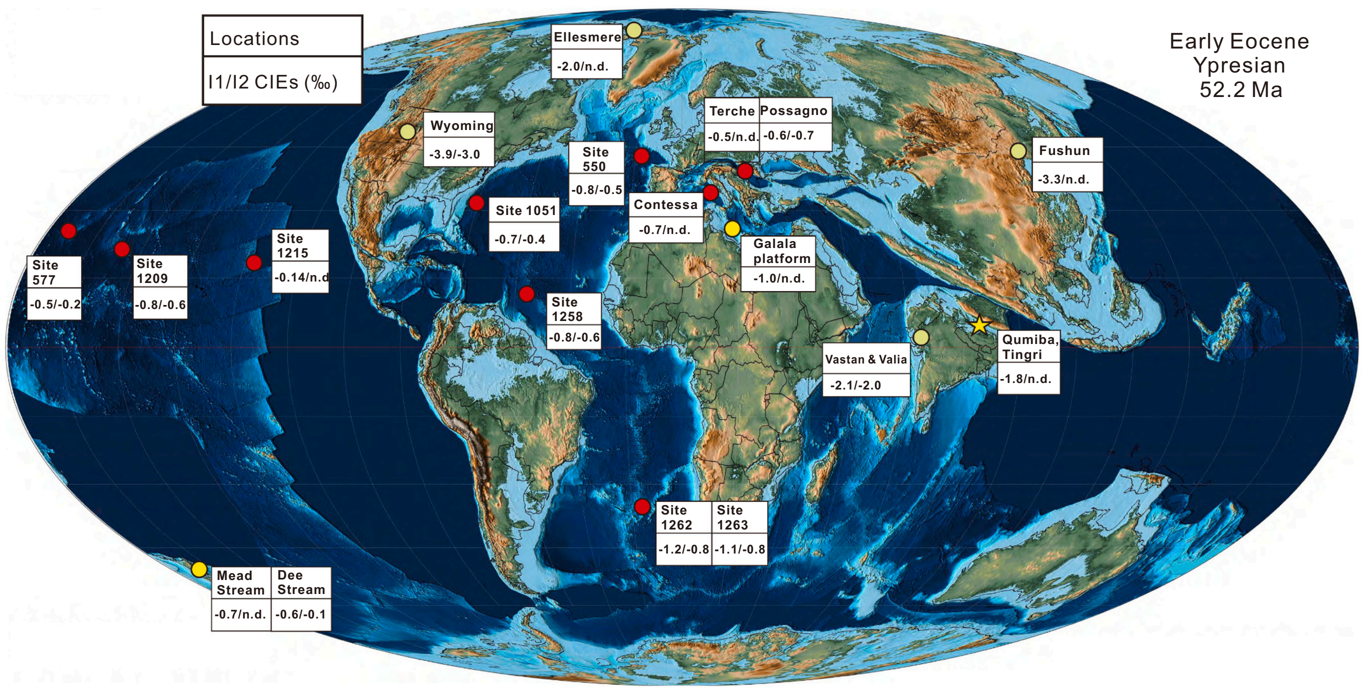

Fig. 8. Global distribution of sites with pelagic-hemipelagic (red symbol), shallow-marine (yellow symbol) and terrestrial (green symbol) carbon isotope data across the hyperthermal events of I1-I2. Numbers: CIE magnitude for I1/I2; n.d.: no data. Paleogeography base map is from Scotese (2014). (For interpretation of the references to colour in this figure legend, the reader is referred to the web version of this article.)

processes and are considered robust and globally representative.

The CIE magnitudes during the I1/I2 between shallow and deep sections also differ. For example, the maximum CIE magnitude of the Qumiba section (~1.8‰) is larger than those in the hemipelagic-pelagic sites (0.2–1.2‰; Cramer et al., 2003; Zachos et al., 2010; Lauretano et al., 2015; Galeotti et al., 2019). Furthermore, the CIE magnitudes of shallow marine records are much smaller than those of terrestrial records (*e.g.,* ~3.3‰ in the Fushun Basin from Chen et al. (2014); ~3.9‰ in the Wyoming Bighorn Basin from Abels et al. (2016)) (Fig. 8; Table S3). This discrepancy can be explained by the amplification of terrestrial CIE from elevated CO_2 and increased water availability (Cui and Schubert, 2017; Schubert and Jahren, 2013). Dissolution of deep-marine carbonates may help explain the smaller CIE magnitudes in the hemipelagic-pelagic sites (Sexton et al., 2006; Thomas et al., 2018; Zachos et al., 2005).

6. Conclusions

Detailed stable isotopes and elemental analyses of the Qumiba section in the southern Tibet allow for the recognition of at least one early Eocene hyperthermal event (I1/I2) and the assessment of associated environmental changes. The negative excursions of $\delta^{13}C_{carb}$ and $\delta^{18}O_{carb}$ (−1.8‰ and −1.7‰ respectively) in Unit 2 and the chemical weathering proxies (*i.e.*, CIA, CIX and PIA values) support ^{13}C-depleted carbon emissions and enhanced chemical weathering. The negative excursion of $\delta^{13}C_{carb}$ in Unit 3 was likely triggered by volcanic activities caused by the incipient India–Asia collision, evidenced by the sharp increase of the Ti_{EF}, Cr_{EF}, Zr_{EF} and Na_2O contents. The volcanic inputs have led to the increase in primary productivity and expansion of anoxic conditions in the bottom waters, evidenced by the paleoproductivity (P_{EF}, Ba_{EF}, Ni_{EF} and Cu_{EF}) and redox proxies (U_{EF}, V_{EF}, and Ce/Ce*). Although the active tectonic movements may affect the isotopic signals of the hyperthermal events, the I1/I2 event before the final closure of the Neo-Tethys Ocean is recognizable through multiple geochemical proxies. The resultant environmental changes are similar to those of the shallow marine settings in other regions globally, offering insights into the impacts of early Eocene hyperthermal events on shallow-marine environments, which provides an ancient analogue for anthropogenic climate change.

Declaration of Competing Interest

The authors declare that they have no known competing financial interests or personal relationships that could have appeared to influence the work reported in this paper.

Acknowledgements

We thank the reviewers for their constructive feedbacks which greatly improved the manuscript. This work was supported by NSF to Y. C. (grant 2002370) and the National Science Foundation of China to S. Jiang (grant numbers 41888101 and 41672004). We thank Yasu Wang, Xu Wen and Yuanda Lei for field work assistance.

Appendix A. Supplementary data

Supplementary data to this article can be found online at https://doi.org/10.1016/j.gloplacha.2022.103875.

References

Abels, H.A., et al., 2012. Terrestrial carbon isotope excursions and biotic change during Palaeogene hyperthermals. Nat. Geosci. 5 (5), 326–329.
Abels, H., et al., 2016. Environmental impact and magnitude of paleosol carbonate carbon isotope excursions marking five early Eocene hyperthermals in the Bighorn Basin, Wyoming. Clim. Past 12 (5), 1151–1163.
Algeo, T.J., Ingall, E., 2007. Sedimentary Corg: P ratios, paleocean ventilation, and Phanerozoic atmospheric pO_2. Palaeogeogr. Palaeoclimatol. Palaeoecol. 256 (3–4), 130–155.
Babechuk, M.G., Widdowson, M., Kamber, B.S., 2014. Quantifying chemical weathering intensity and trace element release from two contrasting basalt profiles, Deccan Traps, India. Chem. Geol. 363, 56–75.

Bau, M., Dulski, P., 1996. Distribution of yttrium and rare-earth elements in the Penge and Kuruman iron-formations, Transvaal Supergroup, South Africa. Precambrian Res. 79 (1–2), 37–55.

Bau, M., Koschinsky, A., 2009. Oxidative scavenging of cerium on hydrous Fe oxide: evidence from the distribution of rare earth elements and yttrium between Fe oxides and Mn oxides in hydrogenetic ferromanganese crusts. Geochem. J. 43 (1), 37–47.

Bhatia, M.R., Crook, K.A.W., 1986. Trace element characteristics of graywackes and tectonic setting discrimination of sedimentary basins. Contrib. Mineral. Petrol. 92 (2), 181–193.

Bown, P., 1998. Calcareous Nannofossil Biostratigraphy. Chapman and Hall; Kluwer Academic.

Chen, J., An, Z., Head, J., 1999. Variation of Rb/Sr ratios in the loess-paleosol sequences of central China during the last 130,000 years and their implications for monsoon paleoclimatology. Quat. Res. 51 (3), 215–219.

Chen, Z., Ding, Z., Tang, Z., Wang, X., Yang, S., 2014. Early Eocene carbon isotope excursions: evidence from the terrestrial coal seam in the Fushun Basin, Northeast China. Geophys. Res. Lett. 41 (10), 3559–3564.

Cramer, B.S., Wright, J.D., Kent, D.V., Aubry, M.P., 2003. Orbital climate forcing of $\delta^{13}C$ excursions in the late Paleocene–early Eocene (chrons C24n–C25n). Paleoceanography 18 (4).

Critelli, S., et al., 2008. Compositional and geochemical signatures for the sedimentary evolution of the Middle Triassic–Lower Jurassic continental redbeds from Western-Central Mediterranean Alpine Chains. J. Geol. 116 (4), 375–386.

Cui, Y., Schubert, B.A., 2017. Atmospheric pCO_2 reconstructed across five early Eocene global warming events. Earth Planet. Sci. Lett. 478, 225–233.

Cullers, R.L., 2002. Implications of elemental concentrations for provenance, redox conditions, and metamorphic studies of shales and limestones near Pueblo, CO, USA. Chem. Geol. 191 (4), 305–327.

Dahl, T.W., Arens, S.K.M., 2020. The impacts of land plant evolution on Earth's climate and oxygenation state–an interdisciplinary review. Chem. Geol. 119665.

Dedert, M., et al., 2012. Productivity response of calcareous nannoplankton to Eocene Thermal Maximum 2 (ETM2). Clim. Past 8 (3), 977–993.

Dellinger, M., Bouchez, J., Gaillardet, J., Faure, L., Moureau, J., 2017. Tracing weathering regimes using the lithium isotope composition of detrital sediments. Geology 45 (5), 411–414.

Ding, L., et al., 2016. The India–Asia collision in north Pakistan: insight from the U–Pb detrital zircon provenance of Cenozoic foreland basin. Earth Planet. Sci. Lett. 455, 49–61.

Dinis, P.A., Garzanti, E., Hahn, A., Vermeesch, P., Cabral-Pinto, M., 2020. Weathering indices as climate proxies. A step forward based on Congo and SW African river muds. Earth Sci. Rev. 201, 103039.

D'Onofrio, R., et al., 2016. Environmental perturbations at the early Eocene ETM2, H2, and I1 events as inferred by Tethyan calcareous plankton (Terche section, northeastern Italy). Paleoceanography 31 (9), 1225–1247.

D'Onofrio, R., Luciani, V., Dickens, G.R., Wade, B.S., Kirtland Turner, S., 2020. Demise of the Planktic Foraminifer Genus Morozovella during the Early Eocene Climatic Optimum: new records from ODP Site 1258 (Demerara Rise, western equatorial Atlantic) and Site 1263 (Walvis Ridge, South Atlantic). Geosciences 10 (3), 88.

Eggleton, R.A., Foudoulis, C., Varkevisser, D., 1987. Weathering of basalt: changes in rock chemistry and mineralogy. Clay Clay Miner. 35 (3), 161–169.

El Bouseily, A.M., El Sokkary, A.A., 1975. The relation between Rb, Ba and Sr in granitic rocks. Chem. Geol. 16 (3), 207–219.

Fedo, C.M., Nesbitt, H.W., Young, G.M., 1995. Unraveling the effects of potassium metasomatism in sedimentary rocks and paleosols, with implications for paleoweathering conditions and provenance. Geology 23 (10), 921–924.

Floyd, P.A., Leveridge, B.E., 1987. Tectonic environment of the Devonian Gramscatho basin, south Cornwall: framework mode and geochemical evidence from turbiditic sandstones. J. Geol. Soc. 144 (4), 531–542.

Francescone, F., et al., 2019. A 9 million-year-long astrochronological record of the early–middle Eocene corroborated by seafloor spreading rates. Bulletin 131 (3–4), 499–520.

Galeotti, S., et al., 2010. Orbital chronology of Early Eocene hyperthermals from the Contessa Road section, central Italy. Earth Planet. Sci. Lett. 290 (1–2), 192–200.

Galeotti, S., et al., 2019. Stratigraphy of early to middle Eocene hyperthermals from Possagno (Southern Alps, Italy) and comparison with global carbon isotope records. Palaeogeogr. Palaeoclimatol. Palaeoecol. 527, 39–52.

Garver, J.I., Scott, T.J., 1995. Trace elements in shale as indicators of crustal provenance and terrane accretion in the southern Canadian Cordillera. Geol. Soc. Am. Bull. 107 (4), 440–453.

Garzanti, E., Padoan, M., Setti, M., López-Galindo, A., Villa, I.M., 2014. Provenance versus weathering control on the composition of tropical river mud (southern Africa). Chem. Geol. 366, 61–74.

German, C.R., Elderfield, H., 1990. Application of the Ce anomaly as a paleoredox indicator: the ground rules. Paleoceanography 5 (5), 823–833.

Hamme, R.C., et al., 2010. Volcanic ash fuels anomalous plankton bloom in subarctic northeast Pacific. Geophys. Res. Lett. 37 (19).

Harper, D.T., et al., 2020. The magnitude of surface ocean acidification and carbon release during Eocene Thermal Maximum 2 (ETM-2) and the Paleocene-Eocene Thermal Maximum (PETM). Paleoceanogr. Paleoclimatol. 35 (2) e2019PA003699.

Hayashi, K.-I., Fujisawa, H., Holland, H.D., Ohmoto, H., 1997. Geochemistry of ~1.9 Ga sedimentary rocks from northeastern Labrador, Canada. Geochim. Cosmochim. Acta 61 (19), 4115–4137.

Hessler, A.M., Zhang, J., Covault, J., Ambrose, W., 2017. Continental weathering coupled to Paleogene climate changes in North America. Geology 45 (10), 911–914.

Höntzsch, S., et al., 2011. Increasing restriction of the Egyptian shelf during the early Eocene?—New insights from a southern Tethyan carbonate platform. Palaeogeogr. Palaeoclimatol. Palaeoecol. 302 (3–4), 349–366.

Horner, T., et al., 2021. Bioactive trace metals and their isotopes as paleoproductivity proxies: an assessment using GEOTRACES-era data. Glob. Biogeochem. Cycles 35 (11) e2020GB006814.

Hoshina, K., et al., 2021. Eocene calcareous nannofossils from southern Tibet: paleoceanographic implications for the closure of the eastern Tethys Ocean. Mar. Micropaleontol. 102031.

Hu, X., Sinclair, H.D., Wang, J., Jiang, H., Wu, F., 2012. Late Cretaceous-Palaeogene stratigraphic and basin evolution in the Zhepure Mountain of southern Tibet: implications for the timing of India-Asia initial collision. Basin Res. 24 (5), 520–543.

Hu, X., et al., 2016. The timing of India-Asia collision onset–facts, theories, controversies. Earth Sci. Rev. 160, 264–299.

Jiang, S., Wise Jr., S.W., 2006. Surface-water chemistry and fertility variations in the tropical Atlantic across the Paleocene/Eocene Thermal Maximum as evidenced by calcareous nannoplankton from ODP Leg 207, Hole 1259B. Rev. Micropaleontol. 49 (4), 227–244.

Jiang, S., Cui, Y., Wang, Y., 2021. Carbon cycle variability in tropical Atlantic across two Early Eocene hyperthermals. Geosci. Front. 12 (2), 521–530.

Jin, Z., Cao, J., Wu, J., Wang, S., 2006. A Rb/Sr record of catchment weathering response to Holocene climate change in Inner Mongolia. Earth Surf. Proc. Landforms J. Brit. Geomorphol. Res. Group 31 (3), 285–291.

Kahn, A., Aubry, M.-P., 2004. Provincialism associated with the Paleocene/Eocene thermal maximum; temporal constraint. In: Villa, G., Lees, J.A., Bown, P.R. (Eds.), Marine Micropaleontology, pp. 117–131.

Kemp, D.B., Selby, D., Izumi, K., 2020. Direct coupling between carbon release and weathering during the Toarcian oceanic anoxic event. Geology 48 (10), 976–980.

Khozyem, H., Adatte, T., Spangenberg, J.E., Tantawy, A.A., Keller, G., 2013. Palaeoenvironmental and climatic changes during the Palaeocene–Eocene Thermal Maximum (PETM) at the Wadi Nukhul Section, Sinai, Egypt. J. Geol. Soc. 170 (2), 341–352.

Kohn, M.J., Parkinson, C.D., 2002. Petrologic case for Eocene slab breakoff during the Indo-Asian collision. Geology 30 (7), 591–594.

Krishnan, S., Pagani, M., Huber, M., Sluijs, A., 2014. High latitude hydrological changes during the Eocene Thermal Maximum 2. Earth Planet. Sci. Lett. 404, 167–177.

Kump, L.R., Brantley, S.L., Arthur, M.A., 2000. Chemical weathering, atmospheric CO_2, and climate. Annu. Rev. Earth Planet. Sci. 28 (1), 611–667.

Lauretano, V., Littler, K., Polling, M., Zachos, J., Lourens, L., 2015. Frequency, magnitude and character of hyperthermal events at the onset of the Early Eocene Climatic Optimum. Clim. Past Discuss. 11 (3).

Lee, H.-Y., et al., 2009. Eocene Neotethyan slab breakoff in southern Tibet inferred from the Linzizong volcanic record. Tectonophysics 477 (1–2), 20–35.

Lei, Y., Jiang, S., Wise Jr., S.W., Cui, Y., Wang, Y., 2016. Contrasting response of the calcareous nannoplankton communities after the Eocene hyperthermal events in the tropical Atlantic Ocean. Mar. Micropaleontol. 129, 24–31.

Leon-Rodriguez, L., Dickens, G.R., 2010. Constraints on ocean acidification associated with rapid and massive carbon injections: the early Paleogene record at ocean drilling program site 1215, equatorial Pacific Ocean. Palaeogeogr. Palaeoclimatol. Palaeoecol. 298 (3–4), 409–420.

Li, J., Hu, X., Garzanti, E., An, W., Wang, J., 2015. Paleogene carbonate microfacies and sandstone provenance (Gamba area, South Tibet): stratigraphic response to initial India–Asia continental collision. J. Asian Earth Sci. 104, 39–54.

Li, J., Hu, X., Garzanti, E., BouDagher-Fadel, M., 2017. Shallow-water carbonate responses to the Paleocene–Eocene thermal maximum in the Tethyan Himalaya (southern Tibet): tectonic and climatic implications. Palaeogeogr. Palaeoclimatol. Palaeoecol. 466, 153–165.

Littler, K., Röhl, U., Westerhold, T., Zachos, J.C., 2014. A high-resolution benthic stable-isotope record for the South Atlantic: implications for orbital-scale changes in Late Paleocene–Early Eocene climate and carbon cycling. Earth Planet. Sci. Lett. 401, 18–30.

Liu, Z., et al., 2017. Paleo-environmental cyclicity in the Early Silurian Yangtze Sea (South China): tectonic or glacio-eustatic control? Palaeogeogr. Palaeoclimatol. Palaeoecol. 466, 59–76.

Mahéo, G., Guillot, S., Blichert-Toft, J., Rolland, Y., Pêcher, A., 2002. A slab breakoff model for the Neogene thermal evolution of South Karakorum and South Tibet. Earth Planet. Sci. Lett. 195 (1–2), 45–58.

McLennan, S.M., 1993. Weathering and global denudation. J. Geol. 101 (2), 295–303.

McLennan, S.M., 1994. Rare earth element geochemistry and the "tetrad" effect. Geochim. Cosmochim. Acta 58 (9), 2025–2033.

McLennan, S.M., 2018. Rare earth elements in sedimentary rocks: influence of provenance and sedimentary processes. Geochem. Mineral. Rare Earth Elements 169–200.

McLennan, S.M., Taylor, S.R., 1991. Sedimentary rocks and crustal evolution: tectonic setting and secular trends. J. Geol. 99 (1), 1–21.

McManus, J., et al., 1998. Geochemistry of barium in marine sediments: implications for its use as a paleoproxy. Geochim. Cosmochim. Acta 62 (21–22), 3453–3473.

Meyers, P., 1994. Preservation of elemental and isotopic source identification of sedimentary organic matter. Chem. Geol. 114 (3–4), 289–302.

Murray, R.W., Buchholtz ten Brink, M.R., Jones, D.L., et al., 1990. Rare earth elements as indicators of different marine depositional environments in chert and shale. Geology 18 (3), 268–271.

Najman, Y., et al., 2010. Timing of India-Asia collision: geological, biostratigraphic, and palaeomagnetic constraints. J. Geophys. Res. Solid Earth 115 (B12).

Najman, Y., et al., 2017. The Tethyan Himalayan detrital record shows that India–Asia terminal collision occurred by 54 Ma in the Western Himalaya. Earth Planet. Sci. Lett. 459, 301–310.
Nakada, R., Takahashi, Y., Tanimizu, M., 2016. Cerium stable isotope ratios in ferromanganese deposits and their potential as a paleo-redox proxy. Geochim. Cosmochim. Acta 181, 89–100.
Nesbitt, H., Young, G., 1982. Early Proterozoic climates and plate motions inferred from major element chemistry of lutites. Nature 299 (5885), 715.
Nesbitt, H.W., Young, G.M., 1984. Prediction of some weathering trends of plutonic and volcanic rocks based on thermodynamic and kinetic considerations. Geochim. Cosmochim. Acta 48 (7), 1523–1534.
Nicolo, M.J., Dickens, G.R., Hollis, C.J., Zachos, J.C., 2007. Multiple early Eocene hyperthermals: their sedimentary expression on the New Zealand continental margin and in the deep sea. Geology 35 (8), 699–702.
Ozaki, K., Tajima, S., Tajika, E., 2011. Conditions required for oceanic anoxia/euxinia: constraints from a one-dimensional ocean biogeochemical cycle model. Earth Planet. Sci. Lett. 304 (1–2), 270–279.
Panahi, A., Young, G.M., Rainbird, R.H., 2000. Behavior of major and trace elements (including REE) during Paleoproterozoic pedogenesis and diagenetic alteration of an Archean granite near Ville Marie, Quebec, Canada. Geochim. Cosmochim. Acta 64 (13), 2199–2220.
Paytan, A., Griffith, E.M., 2007. Marine barite: recorder of variations in ocean export productivity. Deep-Sea Res. II Top. Stud. Oceanogr. 54 (5–7), 687–705.
Pourmand, A., Dauphas, N., Ireland, T.J., 2012. A novel extraction chromatography and MC-ICP-MS technique for rapid analysis of REE, Sc and Y: revising CI-chondrite and Post-Archean Australian Shale (PAAS) abundances. Chem. Geol. 291, 38–54.
Pujol, F., Berner, Z., Stüben, D., 2006. Palaeoenvironmental changes at the Frasnian/Famennian boundary in key European sections: chemostratigraphic constraints. Palaeogeogr. Palaeoclimatol. Palaeoecol. 240 (1–2), 120–145.
Raffi, I., De Bernardi, B., 2008. Response of calcareous nannofossils to the Paleocene-Eocene Thermal Maximum: Observations on composition, preservation and calcification in sediments from ODP Site 1263 (Walvis Ridge — SW Atlantic). Mar. Micropaleontol. 69 (2), 119.
Ravizza, G., Norris, R.N., Blusztajn, J., Aubry, M.P., 2001. An osmium isotope excursion associated with the late Paleocene thermal maximum: evidence of intensified chemical weathering. Paleoceanography 16 (2), 155–163.
Reinhardt, L., et al., 2022. Geochemical indications for the Paleocene-Eocene Thermal Maximum (PETM) and Eocene Thermal Maximum 2 (ETM-2) hyperthermals in terrestrial sediments of the Canadian Arctic. Geosphere 18 (1), 327–349.
Riebe, C.S., Kirchner, J.W., Finkel, R.C., 2004. Erosional and climatic effects on long-term chemical weathering rates in granitic landscapes spanning diverse climate regimes. Earth Planet. Sci. Lett. 224 (3–4), 547–562.
Roser, B.P., Korsch, R.J., 1986. Determination of tectonic setting of sandstone-mudstone suites using SiO_2 content and K_2O/Na_2O ratio. J. Geol. 94 (5), 635–650.
Rowley, D.B., 1996. Age of initiation of collision between India and Asia: a review of stratigraphic data. Earth Planet. Sci. Lett. 145 (1–4), 1–13.
Rullkötter, J., 2006. Organic matter: the driving force for early diagenesis. In: Marine Geochemistry. Springer, pp. 125–168.
Samanta, A., et al., 2013. Do the large carbon isotopic excursions in terrestrial organic matter across Paleocene–Eocene boundary in India indicate intensification of tropical precipitation? Palaeogeogr. Palaeoclimatol. Palaeoecol. 387, 91–103.
Scheffler, K., Hoernes, S., Schwark, L., 2003. Global changes during Carboniferous–Permian glaciation of Gondwana: linking polar and equatorial climate evolution by geochemical proxies. Geology 31 (7), 605–608.
Schoenborn, W.A., Fedo, C.M., 2011. Provenance and paleoweathering reconstruction of the Neoproterozoic Johnnie Formation, southeastern California. Chem. Geol. 285 (1–4), 231–255.
Schoepfer, S.D., et al., 2015. Total organic carbon, organic phosphorus, and biogenic barium fluxes as proxies for paleomarine productivity. Earth Sci. Rev. 149, 23–52.
Schubert, B.A., Jahren, A.H., 2013. Reconciliation of marine and terrestrial carbon isotope excursions based on changing atmospheric CO_2 levels. Nat. Commun. 4, 1653.
Scotese, C.R., 2014. Atlas of Paleogene Paleogeographic Maps (Mollweide Projection), Maps 8–15, vol. 1. The Cenozoic, PALEOMAP Atlas for ArcGIS, PALEOMAP Project, Evanston, IL. https://www.aca-demia.edu/11099001/AtlasofPaleogenePaleogeographicMaps, 2014.
Self-Trail, J.M., Powars, D.S., Watkins, D.K., Wandless, G.A., 2012. Calcareous nannofossil assemblage changes across the Paleocene–Eocene Thermal Maximum: evidence from a shelf setting. Mar. Micropaleontol. 92, 61–80.
Sengör, A., 1979. Mid-Mesozoic closure of Permo-Triassic Tethys and its implications. Nature 279, 590–593.
Sexton, P.F., Wilson, P.A., Norris, R.D., 2006. Testing the Cenozoic multisite composite $\delta^{18}O$ and $\delta^{13}C$ curves: new monospecific Eocene records from a single locality, Demerara Rise (Ocean Drilling Program Leg 207). Paleoceanography 21 (2).
Sheldon, N.D., Tabor, N.J., 2009. Quantitative paleoenvironmental and paleoclimatic reconstruction using paleosols. Earth Sci. Rev. 95 (1–2), 1–52.
Shen, J., et al., 2015. Marine productivity changes during the end-Permian crisis and Early Triassic recovery. Earth Sci. Rev. 149, 136–162.
Slotnick, B.S., et al., 2012. Large-amplitude variations in carbon cycling and terrestrial weathering during the latest Paleocene and earliest Eocene: the record at Mead Stream, New Zealand. J. Geol. 120 (5), 487–505.
Spicer, R.A., et al., 2021. Why the 'Uplift of the Tibetan Plateau' is a myth. Natl. Sci. Rev. 8 (1), nwaa091.
Stap, L., et al., 2010. High-resolution deep-sea carbon and oxygen isotope records of Eocene Thermal Maximum 2 and H2. Geology 38 (7), 607–610.
Sugitani, K., Horiuchi, Y., Adachi, M., Sugisaki, R., 1996. Anomalously low Al_2O_3/TiO_2 values for Archean cherts from the Pilbara Block, Western Australia—possible evidence for extensive chemical weathering on the early earth. Precambrian Res. 80 (1–2), 49–76.
Takahashi, S., et al., 2014. Bioessential element-depleted ocean following the euxinic maximum of the end-Permian mass extinction. Earth Planet. Sci. Lett. 393, 94–104.
Taylor, S.R., McLennan, S.M., 1985. The Continental Crust: Its Composition and Evolution.
Thomas, E., et al., 2018. Early Eocene Thermal Maximum 3: biotic response at Walvis Ridge (SE Atlantic Ocean). Paleoceanogr. Paleoclimatol. 33 (8), 862–883.
Tribovillard, N., Algeo, T., Lyons, T., Riboulleau, A., 2006. Trace metals as paleoredox and paleoproductivity proxies: an update. Chem. Geol. 232 (1–2), 12–32.
Van Cappellen, P., Ingall, E.D., 1996. Redox stabilization of the atmosphere and oceans by phosphorus-limited marine productivity. Science 271 (5248), 493–496.
Von Blanckenburg, F., 2005. The control mechanisms of erosion and weathering at basin scale from cosmogenic nuclides in river sediment. Earth Planet. Sci. Lett. 237 (3–4), 462–479.
Wang, C., Li, X., Hu, X., Jansa, L., 2002. Latest marine horizon north of Qomolangma (Mt Everest): implications for closure of Tethys seaway and collision tectonics. Terra Nova 14 (2), 114–120.
Wang, C., et al., 2008. Constraints on the early uplift history of the Tibetan Plateau. Proc. Natl. Acad. Sci. 105 (13), 4987–4992.
Wang, P., et al., 2020. The chemical index of alteration (CIA) as a proxy for climate change during glacial-interglacial transitions in Earth history. Earth Sci. Rev. 201, 103032.
Wedepohl, K., 1991. The composition of the upper earth's crust and the natural cycles of selected metals. Metal in natural raw materials, natural resources. In: Metals and their compounds in the environment. Occurrence, analysis and biological relevance, pp. 3–17.
West, A.J., Galy, A., Bickle, M., 2005. Tectonic and climatic controls on silicate weathering. Earth Planet. Sci. Lett. 235 (1–2), 211–228.
Westerhold, T., Röhl, U., Donner, B., Zachos, J., 2018. Global extent of early Eocene hyperthermal events: a new Pacific benthic foraminiferal isotope record from Shatsky Rise (ODP Site 1209). Paleoceanogr. Paleoclimatol. 33 (6), 626–642.
Willems, H., Zhou, Z., Zhang, B., Gräfe, K.U., 1996. Stratigraphy of the Upper Cretaceous and lower Tertiary strata in the Tethyan Himalayas of Tibet (Tingri area, China). Geol. Rundsch. 85 (4), 723.
Xu, G., et al., 2017. High-resolution clay mineral and major elemental characterization of a Permian-Triassic terrestrial succession in southwestern China: diagenetic and paleoclimatic/paleoenvironmental significance. Palaeogeogr. Palaeoclimatol. Palaeoecol. 481, 77–93.
Yang, J., Cawood, P.A., Du, Y., Li, W., Yan, J., 2016. Reconstructing Early Permian tropical climates from chemical weathering indices. Bulletin 128 (5–6), 739–751.
Yang, J., et al., 2018. Early Wuchiapingian cooling linked to Emeishan basaltic weathering? Earth Planet. Sci. Lett. 492, 102–111.
Yang, S., et al., 2020. Constraints on the accumulation of organic matter in Upper Ordovician-lower Silurian black shales from the Lower Yangtze region, South China. Mar. Petrol. Geol. 120, 104544.
Young, G.M., Nesbitt, H.W., 1998. Processes controlling the distribution of Ti and Al in weathering profiles, siliciclastic sediments and sedimentary rocks. J. Sediment. Res. 68 (3), 448–455.
Zachos, J.C., et al., 2005. Rapid acidification of the ocean during the Paleocene-Eocene thermal maximum. Science 308 (5728), 1611–1615.
Zachos, J.C., McCarren, H., Murphy, B., Röhl, U., Westerhold, T., 2010. Tempo and scale of late Paleocene and early Eocene carbon isotope cycles: implications for the origin of hyperthermals. Earth Planet. Sci. Lett. 299 (1–2), 242–249.
Zhang, Q., Willems, H., Ding, L., 2013. Evolution of the Paleocene-Early Eocene larger benthic foraminifera in the Tethyan Himalaya of Tibet, China. Int. J. Earth Sci. 102 (5), 1427–1445.
Zhang, Q., Wendler, I., Xu, X., Willems, H., Ding, L., 2017. Structure and magnitude of the carbon isotope excursion during the Paleocene-Eocene thermal maximum. Gondwana Res. 46, 114–123.
Zhang, Q., Willems, H., Ding, L., Xu, X., 2019. Response of larger benthic foraminifera to the Paleocene-Eocene thermal maximum and the position of the Paleocene/Eocene boundary in the Tethyan shallow benthic zones: evidence from south Tibet. Bulletin 131 (1–2), 84–98.
Zhou, L., Friis, H., Poulsen, M.L.K., 2015. Geochemical evaluation of the late Paleocene and early Eocene shales in Siri Canyon, Danish-Norwegian basin. Mar. Pet. Geol. 61, 111–122.
Zhu, B., Kidd, W.S.F., Rowley, D.B., Currie, B.S., Shafique, N., 2005. Age of initiation of the India-Asia collision in the east-central Himalaya. J. Geol. 113 (3), 265–285.
Zhu, R., Zhao, P., Zhao, L., 2021. Tectonic evolution and geodynamics of the Neo-Tethys Ocean. Sci. China Earth Sci. 1–24.